Anomalous cross-field transport in a Hall thruster inferred from direct measurement of instability growth rates

Zachariah A. Brown* and Benjamin A. Jorns
Aerospace Engineering, University of Michigan, Ann Arbor, Michigan 48104, USA

(Received 27 March 2023; accepted 10 October 2023; published 5 December 2023)

The contribution of the electron drift instability to anomalous electron transport is experimentally assessed in a Hall effect discharge. The transport is represented by an anomalous collision frequency, which is related through quasilinear theory to the energy and growth rate of the instability. The wave energy is measured directly with ion saturation probes, while estimates of the growth rate are employed based on both linearized theory and direct measurement. The latter measurement is performed with a bispectral analysis method. The wave-driven collision frequency is compared to measurements of the actual collision frequency inferred from a method based on laser-induced fluorescence. It is found that estimates for transport using linearized theory for the growth differ by over an order of magnitude from the actual anomalous collision frequency in the plasma. The wave-driven anomalous collision frequency with measured growth, however, is shown to agree with the electron collision frequency in magnitude and capture aspects of the trends in spatial variation. This result demonstrates experimentally that wave-driven effects ultimately can explain the observed cross-field transport in these devices. The implications of this finding are discussed in the context of the key lengthscales that drive the transport as well as the implications identifying reduced fidelity models that could be used to predict anomalous collision frequency.

DOI: 10.1103/PhysRevE.108.065204

I. INTRODUCTION

Cross-field electron transport in Hall effect thrusters (HETs) is a poorly understood phenomenon. These axisymmetric devices are characterized by a radial magnetic field crossed with an applied axial electric field. The magnitude of the field strength is tailored such that the electrons are magnetized while the ions are not. As a result, ions are accelerated by the electric field out of the thruster, and most electrons are trapped in an azimuthal Hall effect drift. While classically some electron current parallel to the electric field, i.e., in the cross-field direction, can result from particle-particle collisions, experiments have shown that the actual cross-field current is orders of magnitude higher [1–3]. This so-called "anomalous" transport has yet to be adequately explained. Practically, this lack of understanding has impeded the development of fully predictive Hall thruster models [2,4].

In light of this limitation, several different theories have been proposed to date to explain the transport. These include processes related to Bohm diffusion as well as near-wall effects [3,5–9]. There is a growing consensus, however, that the transport may largely be attributed to the formation of small-scale instabilities [10]. Recent kinetic simulations [11–17] and analytical models [18–20] have suggested that the high $E \times B$ velocity of the electrons results in the growth of the so-called electron drift instability (EDI). This EDI grows at the expense of electron momentum, resulting in an effective drag on this species. This force on the electrons, when combined with the radial magnetic field, promotes a cross-field drift. Indeed, numerical simulations have indicated that this effect may be sufficient to explain the anomalous transport. In parallel, experimental studies have confirmed that the EDI exists in the thruster plasma [21–24]. However, despite this experimental evidence of the EDI, it has yet to be demonstrated if the instability as measured in experiment is sufficient to explain the transport. The role of the EDI in real systems thus remains an open question.

In an effort to address this question, we employed in a previous study experimental measurements of the EDI wave amplitude combined with a linear prediction for the wave growth in an attempt to relate the EDI to an effective transport coefficient. We ultimately found, however, that we were not able to recreate the experimentally measured transport [25]. We subsequently hypothesized that this discrepancy might be attributed to an oversimplification in our approximation of the growth rate, i.e., the rate at which the EDI extracts energy from the Hall drift. Indeed, while we had employed the theoretical form of the growth rate based on a linear expansion of the dielectric response in a Maxwellian plasma, recent simulations have shown that the growth and saturation of the EDI is highly nonlinear in nature [12,13,26]. These nonlinear features in turn can lead to distortion of the electron velocity distribution function (EVDF) and cross-lengthscale coupling, both of which can lower the magnitude of the growth rate and subsequent transport [11,18,20]. In light of these previous modeling results and our direct experimental observation [24] that the EDI growth exhibits nonlinear features, we thus suspected that we would need to amend our estimates for the growth rate in our calculations for EDI-induced transport.

To this end, in our previous work [27] we demonstrated a technique to measure directly the linear growth rates and

*brownzac@umich.edu

nonlinear energy exchange in the Hall thruster acceleration zone, the region of maximum axial electric field, and ion acceleration. The observed nonlinear features indicated the presence of an inverse energy cascade commensurate with results reported in recent simulations of the EDI [12,13], and significantly, the measured linear growth rates were an order lower than values from the idealized linear theory. This result suggests that to make an experimental assessment of EDI-induced transport, it is necessary to employ the directly measured linear growth rates in place of theoretical, linearized values.

The goal of this investigation is to determine the wave-induced transport using direct measurement of the growth rate along the channel centerline of a HET, and to compare the results to the actual cross-field transport. This paper is organized as follows. In Sec. II, we outline the theoretical framework we employ to relate measurements of the EDI to an anomalous transport coefficient. In Sec. III, we detail the experimental setup and methodology for performing measurements of the EDI. In Sec. IV, we present the results of the experiment. In Sec. V, we discuss the results in the context of their implications for our understanding of the role of the EDI in Hall thrusters.

II. THEORY

In this section, we motivate a theoretical and experimental framework for inferring the anomalous transport from measurements of the EDI in a Hall thruster. To this end, we first outline a model for relating plasma instability amplitudes to enhanced transport, and we represent the magnitude of this transport with an anomalous collision frequency. We then review the methodology we use to directly measure the instability's linear growth rates. Finally, we discuss methods for evaluating the expression for anomalous transport in the context of the EDI in Hall thrusters.

A. Relating anomalous collision frequency to EDI properties

Figure 1 shows a representative geometry of a HET. This cylindrical cross-field device features a radial magnetic field, $\vec{B} = B_r\hat{z}$, perpendicular to an applied axial electric field, $\vec{E} = E_{x(0)}\hat{x}$. This field configuration induces an $E \times B$ Hall drift of the electrons in the azimuthal direction, $\hat{y}$. Due to particle-particle collisions, electrons should exhibit some small mobility across magnetic field lines in the direction of the electric field. However, as discussed in the preceding section, the observed electron transport levels are orders of magnitude larger than can be explained by collisions.

The cross-field transport of electrons can be understood by employing the drift-diffusion approximation for electron momentum. This is obtained by neglecting the inertial terms in the electron fluid momentum equation,

$$0 = -\frac{q^2}{m_e} n_e(\vec{E} + \vec{v}_e \times \vec{B}) - \frac{q}{m_e}\nabla(p_e) + \vec{j}_e \nu_c. \tag{1}$$

Here m_e is the electron mass, n_e is the electron density, $\vec{j}_e$ is the electron current density, $\vec{E}$ and $\vec{B}$ are local electric and magnetic fields, $p_e = qn_eT_e$ is electron pressure, where T_e is expressed in units of energy, ν_c is the classical electron momentum transfer collision frequency, and q is the fundamental charge. The first term represents the Lorentz force, the second the pressure force, and the third the effective drag due to particle collisions. We represent the electrostatic EDI waves as rapid perturbations in density, $n_e = \delta n_e + n_{e(0)}$, and electric field, $\vec{E} = \delta\vec{E} + \vec{E}_0$, where $\delta x + x_0$ denotes a quantity x decomposed into an oscillating component δx against a background value x_0. We then phase-average Eq. (1) over the timescale of the oscillation to yield

$$0 = \frac{q^2}{m_e}[\langle \delta n_e \delta\vec{E}\rangle + n_{e(0)}\vec{E}_0 + n_{e(0)}\vec{v}_e \times \vec{B}] - \frac{q}{m_e}\nabla(p_e) - \vec{j}_e\nu_c. \tag{2}$$

In this equation, phase averaging has eliminated the oscillating components of n_e and $\vec{E}$ except for the term containing their product, $\langle \delta n_e \delta\vec{E}\rangle$. If the density and electric field oscillations are in phase, this term will be nonzero.

We next assume that the steady-state electric field is only in the axial direction ($\vec{E}_0 = E_{x(0)}\hat{x}$), while the oscillating electric field induced by the EDI is in the azimuthal direction ($\delta\vec{E} = \delta E_y\hat{y}$). This is in agreement with previous measurements of the EDI propagation vector, where the instability was observed [22,24,28]. Additionally, we take the limit for the radial magnetic field strength to be large enough that the electron cyclotron frequency ($\omega_{ce} = qB_r/m_e$) is much larger than the classical particle collision frequency to arrive at an equation for axial electron current density,

$$j_{e(x)} = \frac{q^2 n_{e(0)}}{m_e\omega_{ce}^2}\left(E_{0(x)} + \frac{\nabla_x(n_{e(0)}T_e)}{n_{e(0)}}\right)\nu_e, \tag{3}$$

where we have defined a total electron collision frequency, $\nu_e = \nu_c + \nu_{AN}$. The latter parameter represents an effective anomalous collision frequency that arises from the action of the waves:

$$\nu_{AN} = -\omega_{ce}\frac{\langle \delta n_e \delta E_y\rangle}{n_{e(0)}E_{x(0)} + \nabla_x(n_{e(0)}T_e)}. \tag{4}$$

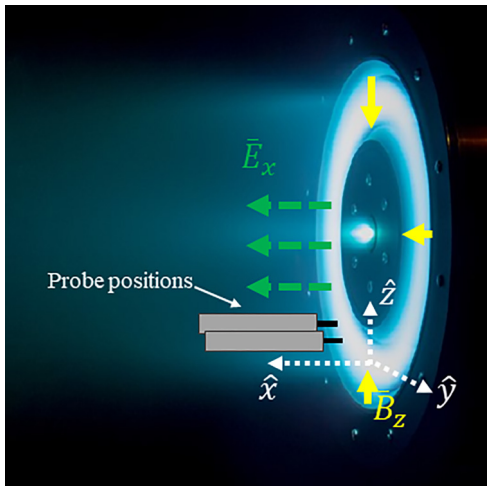

FIG. 1. H9 Hall thruster operating at 300 V and 15 A with an axial electric field ($\bar{E}$) and a radial magnetic field ($\bar{B}$). The coordinate convention and notional orientation of probes in the $E \times B$ direction are also shown.

This definition underscores the fact that from a fluid, phase-averaged perspective, the propagation of the EDI can be represented as an enhanced transport coefficient for the electrons. Similarly, per the definition, we see that as the relative fluctuations in electric field and density from the waves increase, the wave-induced cross-field transport on the electrons will be higher. Physically, this scaling stems from the fact that the growth of the EDI can be interpreted as an effective drag on the azimuthal drift in the plasma, which in turn promotes cross-field current.

In practice, it is prohibitively difficult in our plasma to measure the fluctuating density and the electric field simultaneously for the purpose of evaluating Eq. (4) directly. Instead, we follow a linearized theory for wave propagation where we assume the EDI oscillations can be represented as a summation over a spectrum:

$$\delta\vec{E} = -i\sum_{\vec{k}} \vec{k}\phi(\vec{k},\omega), \tag{5}$$

where $\phi(\vec{k},\omega)$ denotes the propagating oscillations in plasma potential associated with the wave number (k) and frequency (ω) of the electrostatic wave. We invoke in turn the eikonal approximation to write

$$\phi(\vec{k},\omega) = \hat{\phi}(\vec{k},\omega)\exp[i(\vec{k}\cdot\vec{r}-\omega t)], \tag{6}$$

where $\hat{\phi}(\vec{k},\omega)$ denotes the complex amplitude of the potential oscillation.

Following the technique of Davidson and Krall [29], we can then show from a linearization of the dielectric function of the plasma that averaging over the wave phase yields

$$\langle \delta n_e \delta E_k\rangle = \sum_k \gamma_{e(k)} k_y k^2 \frac{\partial \epsilon_r^{(1)}(\vec{k},\omega)}{\partial\omega}|\hat{\phi}(\vec{k},\omega)|^2. \tag{7}$$

Here k_y denotes the component of the wave vector of the kth mode in the Hall direction, $\epsilon_r^{(1)}(\vec{k},\omega)$ is the real component of the dielectric response of the wave to the first order, ω is the real component of the frequency, and we have performed the summation over a spectrum of oscillations associated with the EDI. We have also introduced the parameter $\gamma_{e(k)} = -\epsilon_{i(e)}^{(1)}(\vec{k},\omega)/(\frac{\partial\epsilon_r^{(1)}(\vec{k},\omega)}{\partial\omega})$, which is the linear growth rate of the wave due to the electron contribution to the imaginary component, $\epsilon_{i(e)}^{(1)}(\vec{k},\omega)$, of the dielectric function to the first order. Physically, this latter parameter represents the rate at which electrons extract energy from the Hall drift.

As an additional simplification, we make the substitution $\phi(\vec{k},\omega)/T_e = \delta n_{i(k)}/n_{i(0)}$, where T_e is the electron temperature in electron volts, and $\delta n_{i(k)}$ is the variation in ion density associated with the kth element of this spectrum of the EDI. This relationship is appropriate for the EDI dispersion [19,27] for cold ions, $T_i \ll T_e$, where T_i is the ion temperature. Invoking this simplification, we can express Eq. (4) as

$$\nu_{AN} = \frac{\omega_{ce}}{E_{x(0)} + \frac{\nabla_x(n_{e(0)}T_e)}{n_{e(0)}}} T_e\lambda_{\mathrm{De}}^2 \times \sum_k \gamma_{e(k)} k_y k^2 \frac{\partial\epsilon_r^{(1)}(\vec{k},\omega)}{\partial\omega}\left|\frac{\delta n_{i(k)}}{n_{i(0)}}\right|^2, \tag{8}$$

where λ_{De} denotes the Debye length. This result shows that as the relative fluctuation in ion density increases (an indication of stronger waves), the effective drag on the electrons increases. Similarly, with a higher electron growth rate, i.e., the rate at which the waves extract momentum from the Hall drift, the transport coefficient also increases.

As a final simplification, we note that while Eq. (8) is formulated in terms of a summation over the wave number, in practice our experimental measurements are time-based Fourier transforms of density fluctuations. To translate this result into a form that is experimentally tractable, we assume that the relationship between frequency and wave number is approximately one-to-one such that the kth wave number maps to a unique real frequency, $f = \omega/2\pi$. We therefore can make the substitutions $k \to k_f$, $\delta n_{i(k)} \to \delta n_{i(f)}$, and $\gamma_{e(k)} \to \gamma_{e(f)}$ to find

$$\nu_{AN} = \frac{\omega_{ce}}{E_{x(0)} + \frac{\nabla_x(n_{e(0)}T_e)}{n_{e(0)}}} T_e\lambda_{\mathrm{De}}^2 \times \sum_f \gamma_{e(f)} k_{y(f)} k_f^2 \frac{\partial\epsilon_r^{(1)}(\vec{k},\omega)}{\partial\omega}\left|\frac{\delta n_{i(f)}}{n_{i(0)}}\right|^2. \tag{9}$$

This result ultimately is the expression we experimentally evaluate in order to relate the EDI properties to cross-field transport in the Hall thruster.

B. Theoretical dispersion and growth of the EDI

To estimate the transport coefficient experimentally from Eq. (9), we require measurements of both the dispersion and growth of the EDI. As a first-order approach to determine these properties, we consider the theoretical form of the EDI dispersion that stems from a linearization of the Vlasov equation subject to the assumption of cold ions and Maxwellian electrons [18,19]:

$$\epsilon^{(1)}(\vec{k},\omega) = 1 + k^2\lambda_{\mathrm{De}}^2 + g\left(\frac{\omega - k_y V_{E\times B}}{\omega_{ce}}, \left(k_x^2+k_y^2\right)\rho^2, k_z^2\rho^2\right) - \frac{k^2\lambda_{\mathrm{De}}^2\omega_{pi}^2}{(\omega - k_x v_{i(o)})} = 0 \tag{10}$$

where $g(\Omega, X, Y)$ is the Gordeev function, defined as

$$g(\Omega, X, Y) = i\Omega\int_0^{+\infty} e^{-X[1-\cos(\varphi)]-\frac{1}{2}\varphi^2+i\Omega\varphi}d\varphi. \tag{11}$$

Here ω_{pi} is the ion plasma frequency, $k = \sqrt{k_x^2+k_y^2+k_z^2}$ is the oscillation wave number, $v_{i(0)}$ is the ion beam velocity in the axial direction, $V_{E\times B}$ is the azimuthal Hall drift of the electrons, and $\rho = V_{\mathrm{the}}/\omega_{ce}$ is the electron Larmor radius at thermal velocity, $V_{\mathrm{the}} = \sqrt{qT_e/m_e}$. We show in Fig. 2 example solutions to this dispersion relation, adapted from Ref. [19], for different assumed radial wave numbers.

In Fig. 2(a), we see that the growth rate exhibits periodic peaks when the radial wave number is small. The first and weakest of these peaks corresponds to the so-called modified two-stream instability (MTSI) [12,13] while the subsequent peaks are harmonics of the electron cyclotron resonance frequency, $k_y = n\omega_{ce}/V_{E\times B}$, where n is the harmonic mode number. Figure 2(b) shows that the real frequency is

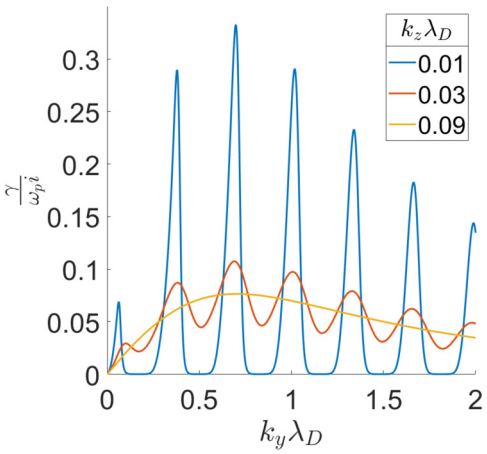

(a)

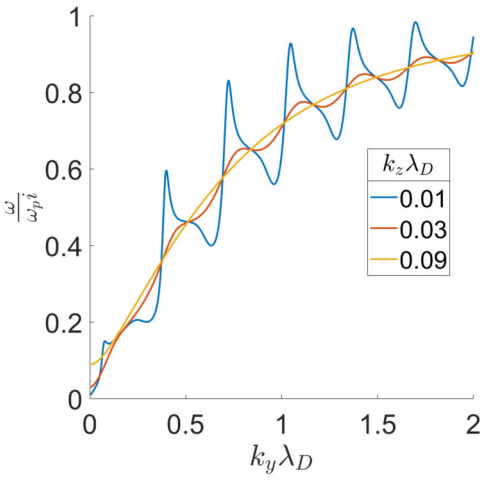

(b)

FIG. 2. Solutions of the EDI dispersion relation, adapted from Cavalier *et al.* [19] with different radial wave components (k_z). Frequency (a) and growth rate (b) are normalized by the ion plasma frequency (ω_{pi}), and wave number is normalized by the Debye length (λ_{De}).

approximately linear, but with periodic peaks in between the cyclotron harmonics. As the radial wave number decreases, the peaks in both the real frequency and the growth rate reduce in amplitude and ultimately disappear. In this limit, the EDI exhibits an ion-acoustic-like dispersion [19].

Previous experimental work has shown that at high frequency (above 2 MHz) and in regions downstream of the acceleration zone, the real components of the wave dispersion in a Hall thruster match the EDI in the acoustic limit [21]. We also demonstrated in recent experimental work that this real part of this dispersion relation is consistent with measurements of the wave propagation in the thruster acceleration zone, but with visible cyclotron harmonics in the power spectrum [24]. The real frequency of the EDI at the cyclotron harmonics remains the same as the wave radial changes and transitions to the ion acoustic solution. In turn, we employ in this work the theoretical form of the real component of the dielectric response in the acoustic limit to evaluate Eq. (9). Given that this dispersion has a one-to-one relationship between frequency and wave number, we similarly can justify the conversion we made in the preceding section, although later in Sec. IV B we estimate the theoretical collision frequency using the imaginary component of full EDI dispersion relation, Eq. (10).

With respect to the growth rate, previous numerical studies and our experimental work have shown that the linearized theory does not accurately reflect the evolution of the EDI [30]. This disparity likely stems from nonlinear effects impacting the wave growth and the kinetic velocity distribution of electrons. With this in mind, while we still use the linear theory as a point of comparison for estimating the transport in this work, we discuss in the following section a methodology we developed to directly measure this growth rate.

C. Technique for directly inferring growth of the EDI

To experimentally estimate the electron growth rate contribution to Eq. (9), we adapted in Ref. [27] the bispectral analysis and experimental method of Ritz [31] and Kim [32]. Following this approach, we consider a governing equation for the temporal-spatial evolution of plasma potential oscillations, $\phi(\vec{k},\omega)$, in frequency and wave-number space:

$$\frac{\partial\phi(\vec{k},\omega)}{\partial t}+\vec{v}_g\cdot\frac{\partial\phi(\vec{k},\omega)}{\partial\vec{r}}=\gamma_k\phi(\vec{k},\omega)+i(\vec{k}\cdot\vec{v}_g-\omega)\phi(\vec{k},\omega)+\sum_{\substack{\omega=\omega_1+\omega_2\\ \vec{k}=\vec{k}_1+\vec{k}_2}}V^Q_{1,2}\phi(\vec{k}_1,\omega_1)\phi(\vec{k}_2,\omega_2). \tag{12}$$

The first term on the left-hand side represents the change of the mode in time, while the second term describes the convection in space at the group velocity $\vec{v}_g=-\partial_{\vec{k}}\epsilon_r^{(1)}(\vec{k},\omega)/\partial_\omega\epsilon_r^{(1)}(\vec{k},\omega)$. On the right-hand side, the first term denotes the total linear growth of the wave $\gamma_k=-\epsilon_i^{(1)}(\vec{k},\omega)/\partial_\omega\epsilon_r^{(1)}(\vec{k},\omega)$. This growth rate is a result of contributions from both electrons and ions, $\gamma_k=\gamma_{e(k)}+\gamma_{i(k)}$. It impacts primarily the amplitude of the mode as it evolves in the plasma. The second term in Eq. (12) represents the evolution of the rapidly varying phase of the mode. It can be related in turn to the real component of the dispersion. The third term models the change in the mode due to three-wave coupling interactions that satisfy $\vec{k}=\vec{k}_1\pm\vec{k}_2$ and $\omega=\omega_1\pm\omega_2$. The coefficient $V^Q_{1,2}$ is a weighting function for the strength of each three-wave interaction, and it is related to the second-order dielectric response [33].

Following the procedure discussed in Ref. [28], we Fourier transform Eq. (12) with respect to time and then discretize it with respect to spatial location:

$$Y_f=L_fX_f+\sum_{f=f_1+f_2}Q_f^{1,2}X_{f_1}X_{f_2}, \tag{13}$$

where $X_f=\hat{\phi}_f(y)$ and $Y_f=\hat{\phi}_f(y+\Delta y)$ denote time-based Fourier transforms of measured plasma potential oscillations at two locations spaced by Δy in the azimuthal direction (Fig. 1). Following the same assumptions discussed in the preceding sections, we have made the approximation that each set of wave vectors, $\vec{k}_1,\vec{k}_2$, map to unique frequencies, f_1, f_2, such that the summation over the second-order term is only

over the frequency domain. We have defined in this expression the linear, L_f, and nonlinear, Q_f, transfer functions that dictate how the amplitude and phase of oscillations change as the wave propagates between the two measurement points. These functions are related to the EDI properties by

$$L_f = [(\gamma_{f(y)}/v_{g(y)} + ik_y)\Delta y + 1 - i\Delta\Theta_f]e^{i\Delta\Theta_f}, \tag{14}$$

$$Q_f^{1,2} = e^{i\Delta\Theta_f} V_{1,2}^Q \Delta y / v_{g(y)}. \tag{15}$$

Here $\Delta\Theta_f$ is the phase difference between the two measurement points for oscillations at frequency, f, and it is determined from the measured cross-power spectrum, $\exp(i\Delta\Theta_f) = Y_f X_f^*/|Y_f X_f^*|$. The term $\gamma_{f(y)}$, which we denote as the "azimuthal" growth rate, represents the projection of the total growth in the azimuthal direction:

$$\gamma_{f(y)} = \gamma_f - \frac{1}{2|X_f|^2}(v_{g(x)}\partial_x|X_f|^2 + v_{g(z)}\partial_z|X_f|^2). \tag{16}$$

The "azimuthal" nomenclature stems from the fact that we are only measuring wave properties as they propagate in this direction. The other two terms in Eq. (16) represent the change in amplitude of the mode in the two directions orthogonal to the measurement.

The azimuthal growth can be determined from the definition of Eq. (14) provided Δy, $\Delta\Theta_f$, $v_{g(y)}$, and L_f are known. With Δy defined by the experimental setup, $\Delta\Theta_f$ determined by calculation of the cross-spectrum ($Y_f^* X_f$), and $v_{g(y)}$ estimated by the theoretical dispersion, the only unknown is the linear transfer function. The procedure for calculating L_f from our measured values of X_f and Y_f, which was originally developed by Ritz [34], involves taking additional moments of Eq. (13) with either X_f, Y_f, or their complex conjugates to form a system of equations:

$$\langle Y_f X_f^* \rangle = L_f \langle X_f X_f^* \rangle + \sum_{f=f_1+f_2} Q_f^{1,2} \langle X_{f_1} X_{f_2} X_f^* \rangle, \tag{17}$$

$$\langle Y_f X_{f1}^* X_{f2}^* \rangle = L_f \langle X_f X_{f1}^* X_{f2}^* \rangle + \sum_{f=f_1+f_2} Q_f^{1,2} \langle X_{f_1} X_{f_2} X_{f1}^* X_{f2}^* \rangle. \tag{18}$$

Here $\langle\rangle$ denotes ensemble averaging over multiple measurements or realizations. Ritz showed that over 1000 realizations are needed to accurately determine the higher-order bispectral terms, e.g., $\langle Y_f X_{f1}^* X_{f2}^* \rangle$ [34]. This system can be inverted after measuring the bispectral terms to solve for L_f and $Q_f^{1,2}$.

As discussed in Ref. [32], this technique is susceptible to several inaccuracies when applied to noisy experimental data. The Kim method improves on the Ritz technique by separating the measured spectral content into a summation of ideal terms driven solely by Eq. (13) and nonideal terms that come from both systematic errors and plasma processes that do not follow Eq. (13):

$$X_f = \beta_f + X_f^{ni}, \; Y_f = \alpha_f + Y_f^{ni}. \tag{19}$$

Here β and α are the ideal terms, and X^{ni} and Y^{ni} are the nonideal terms. With the introduction of the nonideal terms, an additional equation is needed for closure of the system of equations. Kim solved this closure problem by invoking a hypothesis of local stationarity: $\langle \alpha_f \alpha_f^* \rangle = \langle \beta_f \beta_f^* \rangle$. This is justified in our experiment by the azimuthal symmetry of the Hall thruster plasma. It was this technique that we ultimately use to determined L_f and then $\gamma_{f(y)}$.

Once we have measured the azimuthal growth rate, we can relate it in turn to the total growth rate through Eq. (16) provided we characterize the evolution of the magnitude of the wave amplitude as it evolves in the radial and axial directions. We neglect in this work the radial convective term due to symmetry, but we do measure the change in power spectrum amplitude with axial location such that we approximate

$$\gamma_f = \gamma_{f(y)} + \frac{1}{2|X_f|^2}(v_{i(0)}\partial_x|X_f|^2), \tag{20}$$

where we have made the assumption that for the EDI the axial group velocity is the axial ion beam velocity [19]. Equation (20) is the form we employ to measure the total EDI growth rate as a function of frequency in the thruster plasma.

D. Relating total measured EDI growth to electron contribution to growth

As a final step in our methodology, we remark that the procedure outlined in the preceding yields the total growth rate of the waves. However, in order to determine the impact on the electron transport from Eq. (9), we must isolate the electron contribution: $\gamma_{e(f)} = \gamma_f - \gamma_{i(f)}$. This requires that we have an estimate for the ion growth. We consider two possibilities for this ion contribution. The first is based on the linearized dispersion shown in Eq. (10), which is derived under the assumption that the ions are cold. In this case, we can infer from the derivation of this dispersion that $\gamma_{i(f)} = 0$, i.e., that our measured growth is the same as the electron growth. As a second possibility, it has been shown that in the near plume of the Hall thruster, ion temperatures can become sufficiently high that ion Landau damping may become significant [35]. In this case, it is necessary to include a kinetic correction to the EDI dispersion for the ions [36], which in turns yields the approximation

$$\gamma_{i(f)} = -\sqrt{\frac{\pi}{8}} \frac{k_f c_s}{\left(1 + k_f^2 \lambda_{\mathrm{De}}^2\right)^2} \left(\frac{T_e}{T_i}\right)^{3/2} e^{\left[\frac{-T_e}{2T_i(1+k_f^2\lambda_D^2)}\right]}. \tag{21}$$

We add the ion Landau damping rate to the measured total growth rate to determine the electron growth rate:

$$\gamma_{e(f)} = \gamma_{f(y)} + \gamma_{i(f)} + \frac{1}{2|X_f|^2}(v_{i(0)}\partial_x|X_f|^2). \tag{22}$$

We consider in the following both cases for the ion growth rate, referring to them as "with ion Landau damping" and "without ion Landau damping."

In summary, we have established in the preceding section the theoretical framework for relating measurements of the EDI to effective cross-field transport. This technique requires experimental characterization of the complex spectra of oscillations at multiple locations in the plasma as well as estimates of the background plasma properties. We discuss our techniques for measuring these properties in the following.

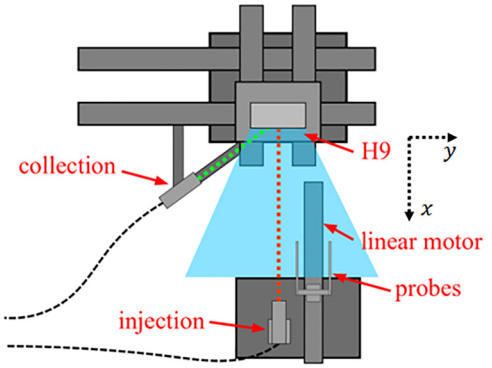

FIG. 3. Schematic of the experimental setup showing the H9 Hall thruster with respect to the LIF optics and wave probes mounted on a fast motion stage.

III. EXPERIMENTAL SETUP

In this section, we describe the thruster and test facility that we employed for our experiment. We then summarize our diagnostic techniques for measuring the plasma oscillations as well as background plasma parameters.

A. Test article

We performed this experimental campaign with the H9 (Fig. 1), a 9-kW class HET developed jointly by NASA's Jet Propulsion Laboratory, the University of Michigan, and the Air Force Research Laboratory [37,38]. The H9 employs a magnetically shielded topography [39] and uses a center-mounted LaB_6 hollow cathode that is electrically connected to the thruster's main body. We characterized this thruster in the Large Vacuum Test Facility (LVTF) at the University of Michigan. This is a 6 m × 9 m cryogenically pumped steel vacuum test chamber. The H9 was operated at 300 V discharge voltage and 15 A discharge current with a xenon flow rate of 165 sccm through the anode and a 7% cathode flow fraction. The facility pressure was 3×10^{-6} Torr-xenon during testing as measured in the plane of the thruster.

B. Diagnostics

We employed two key diagnostics in our experiment: ion saturation probes to characterize the plasma density fluctuations, and laser-induced fluorescence (LIF) to measure the local ion velocity distribution function. Figure 3 shows the experimental layout for these diagnostics with respect to the H9. We describe in the following the key properties of these measurement techniques as well as our analysis methods for extracting plasma properties from the measurements.

1. Ion saturation probes

We employed two ion saturation probes for measuring the fluctuations in ion density locally in the thruster plasma. The probes consisted of 0.38 mm radius tungsten rods with an exposed length of 3.8 mm. These cylindrical probes were separated azimuthally by 1 cm and mounted on fast motion stages to quickly inject the probes in the plume and minimize perturbative effects. The probes collected data at fixed locations along the channel centerline from $x/L_{\mathrm{ch}} = 0.125$ to 0.75 downstream of the thruster exit plane, where L_{ch} denotes the axial length of the thruster, and $x = 0$ corresponds to the anode face. The ion saturation probes were biased to −45 V with respect to the ground in order to collect only ion current. The current was converted into a voltage reading across a low-inductance and low-capacitance 100Ω resistor and then read by an ATS9462 16-bit digitizer. The signal was sampled at 100 MHz for two megasamples, and the resulting waveform was then subdivided into 2000 realizations for averaging. The fluctuations in ion saturation, δi, were related to fluctuations in ion density with the relation $\delta i/i_0 \approx \delta n_i/n_{i(0)}$, where i_0 denotes the time-averaged ion saturation current. This relationship is based on the assumption that the electron temperature remains approximately constant on the timescale of the EDI fluctuations [24].

As we discuss in Sec. III B 3, the ion saturation probes also provided an estimate of the downstream plasma density for use as a boundary condition in calculating the axial ion density profile. We determined the time-averaged ion density from the measured ion saturation current in this case from [40]

$$n_{i(0)} = \frac{i_{\mathrm{sat}}}{qA_p c_s \exp(1/2)}, \tag{23}$$

where A_p is the probe area and $c_s = \sqrt{qT_e/m_i}$ is the ion sound speed. The electron temperature in this expression was inferred using the LIF technique outlined in Sec. III B 3.

2. Laser-induced fluorescence

Laser-induced fluorescence is a noninvasive optical technique for measuring projections of the ion velocity distribution functions (IVDFs). For this experiment, we used the experimental configuration described in detail in Ref. [41]. In brief, our system employed the $5d[4]_{7/2} - 6p[3]_{5/2}$(834.72 nm) transition for singly charged xenon (Xe II). The laser was injected parallel to the thruster centerline and focused to a 1 mm^3 point (Fig. 3). The fluorescence from this spot induced by the laser was collected by optics offset 60° from the laser axis. By tuning the wavelength of the laser and monitoring the amplitude of the fluoresced signal, we were able in turn to infer the ion velocity distribution function along the direction of the beam, i.e., in the axial direction. We show in Fig. 4 an example measurement of the IVDF in the downstream Hall thruster plume where ions have been accelerated to a mean velocity of 16 km/s. We generated spatially resolved measurements of this IVDF by translating the thruster with respect to the intersection point of the injection and collection optics. Our measurement domain ranged from $x/L = 1.0$ to 1.75 with a spatial resolution of $\Delta x/L = 0.025$. As discussed in Ref. [41], nonideal effects like Zeeman splitting contribute <10% when computing moments on the IVDF. We neglect this relatively minor degree of uncertainty in our analysis.

3. IBIS method

While LIF directly yields measurements of the IVDF, we were able to use this technique to infer noninvasively a number of other key properties in the plasma discharge. This is a critical capability as it has been shown that conventional swept probes, when inserted into a Hall thruster discharge,

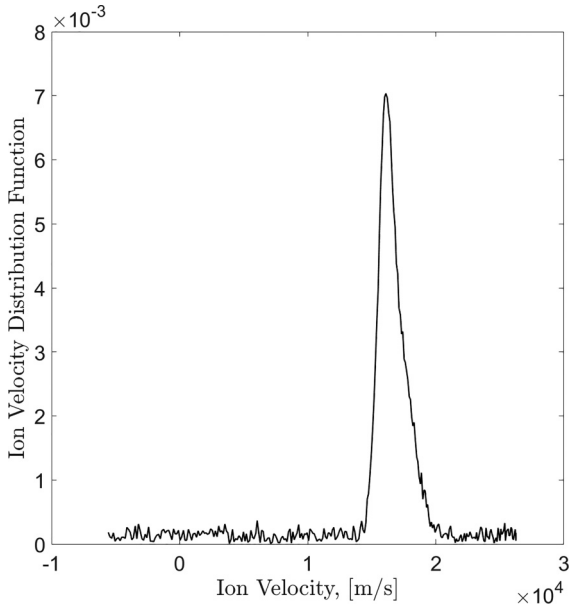

FIG. 4. Example ion velocity distribution function measured by LIF.

can perturb the local plasma state [42,43]. Our method for employing LIF for this purpose, which is based on the works of Perez-Luna *et al.* and Dale and Jorns, yielded estimates for plasma density, electric field, electron temperature, ion beam velocity, and anomalous collision frequency [41,44]. We briefly review in the following the key elements of this approach.

This analysis method, which was termed the ion Boltzmann implicit solution method (IBIS) by Dale and Jorns [41], starts with the 1D ion Boltzmann equation for the IVDF in the axial direction:

$$\frac{\partial f}{\partial t} + u_i \frac{\partial f}{\partial x} + \frac{q}{m_i} E_{x(0)} \frac{\partial f}{\partial v_i} = \left(\frac{\partial f}{\partial t}\right)_{iz}. \tag{24}$$

In this equation, u_i is the independent axial ion velocity, $v_{i(0)} = \int u_i f du_i / n_{i(0)}$, and the rightmost term is the time rate of change in the IVDF due to ionization. Assuming the IVDF is at steady state on the timescale of the background plasma properties, the zeroth-, first-, and second-order moments of the Boltzmann equation yield the following fluid equations:

$$\frac{\partial \overline{u_i} n_{i(0)}}{\partial x} = n_i f_{iz}, \tag{25}$$

$$\frac{\partial \overline{u_i^2} n_{i(0)}}{\partial x} - \frac{q}{m} n_{i(0)} E_x = 0, \tag{26}$$

$$\frac{\partial \overline{u_i^3} n_{i(0)}}{\partial x} - 2\frac{q}{m} n_{i(0)} E_{x(0)} \overline{v_i} = 3\frac{q}{m_i} T_i n_{i(0)} f_{iz}. \tag{27}$$

Here $\overline{u_i^y} = \int u_i^y f du_i / n_{i(0)}$, f_{iz} is the ionization frequency, and T_i is the temperature of newly born ions, which we assume is equal to the neutral gas temperature. With the spatial resolved LIF measurements, this system can be solved for $E_{x(0)}$, f_{iz}, and $d \ln (n_{i(0)})/dx$. This last variable can then be integrated across the axial domain to determine the ion density if the density is known at one of the boundary points x_b:

$$n_{i(0)}(x) = -\exp\left[\int_{x_b}^{x} \frac{d \ln n_{i(0)}}{dx}\right] + n_{i(0)}(x_b). \tag{28}$$

This downstream density $[n_{i(0)}(x_b)]$ is estimated with the wave probes that also function as ion saturation probes for measuring ion density. With this information, in addition to the value of the applied magnetic field, we can calculate the effective total electron collision frequency ($\nu_e = \nu_c + \nu_{AN}$) using Ohm's law,

$$\nu_e = \frac{\Xi \pm \sqrt{\Xi^2 - [2 v_{\mathrm{ex}(0)} B_r]^2}}{2\frac{m_e}{e} v_{\mathrm{ex}(0)}}, \tag{29}$$

where $v_{\mathrm{ex}(0)}$ is the axial electron velocity, and we define $\Xi = E_{x(0)} + \frac{\nabla n_{e(0)} T_e}{n_{e(0)}} - \eta_i j_i$, where $\eta_i = m_i \nu_c / q^2 n_{i(0)}$ is the classical ion resistivity due to collisions and j_i is the ion current density. All parameters in Eq. (29) are determined from the solution of Eqs. (25)–(27) except for the classical collision frequency, the axial electron velocity, and the electron temperature.

We determine the electron temperature from the calculated ionization frequency f_{iz} using tabled values of the ionization rate $\xi_i(T_e) = f_{iz}/n_n$, where n_n is the neutral density (cf. Ref. [45]), although this technique requires an estimation of the neutral density profile. We calculate the neutral density using the conservation equations for the neutral fluid combined with our calculated ionization frequency and an estimate of the downstream neutral density. The boundary condition for the neutral density was guided by previous experimental measurements in the literature [46].

The axial electron velocity is determined through the ion and electron continuity equations. If the ions and electrons are restricted to one-dimensional (axial) flow, the electron current density is the difference between the total discharge current density j_d and the ion current density: $j_e = j_d - j_i$. While the ion current density is known from the measured beam velocity and plasma density, the discharge current density is assumed to be the total discharge current (I_d) uniformly distributed over the channel area, A_{ch}, of the thruster: $j_d = I_d / A_{\mathrm{ch}}$. Subject to these assumptions, the electron velocity is given by

$$v_{\mathrm{ex}(0)} = \frac{I_d}{n_{i(0)} A_{\mathrm{ch}}} - v_{i(0)}, \tag{30}$$

where we have assumed $n_{e(0)} \approx n_{i(0)}$ by quasineutrality.

Finally, the classical collision frequency is calculated using the Spitzer collision frequency equations for electron-neutral and electron-ion collisions (cf. Ref. [45]). Therefore, the IBIS method provides an estimate of anomalous collision frequency by subtracting the classical collision frequency from the calculated total collision frequency in Eq. (29). This serves as a baseline value against which we shall compare our wave-driven collision frequencies. Additionally, the background plasma parameters determined by the IBIS method can be used to solve the dispersion relation of the EDI for estimating a theory-driven anomalous collision frequency and a group velocity for use in the Ritz and Kim technique when determining $\gamma_{f(y)}$.

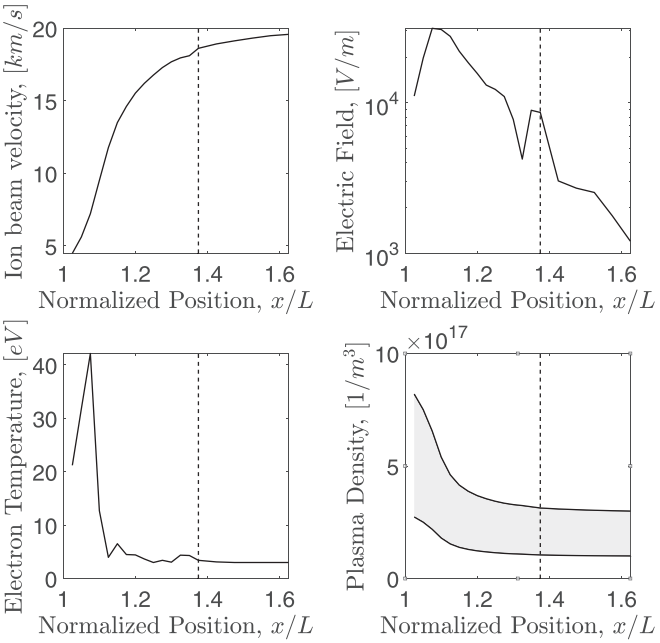

FIG. 5. Plasma properties inferred from LIF measurements. (a) Ion beam velocity, (b) axial electric field, (c) electron temperature, and (d) ion density as a function of axial position normalized by the channel length, where $x/L = 1$ is the exit plane of the thruster. The dashed vertical line at $x/L = 1.375$ denotes the location of the peak radial magnetic field strength.

IV. RESULTS

In this section, we present the experimental results of our study. We first show the background plasma parameters we determined from the IBIS technique. We then present the properties of the EDI, including the measured power spectra and growth. We conclude with a comparison of the measured collision frequency to the EDI-induced collision frequency.

A. Background plasma properties

We show in Fig. 5 four key plasma parameters inferred from the IBIS method—ion velocity, electron temperature, electric field strength, and plasma density—as a function of axial distance from the anode normalized by the channel length, L. For reference, we also show in these figures as a vertical line the location of peak magnetic field. As can be seen from Fig. 5(a), the ion velocity increases monotonically with position, with the majority of acceleration occurring between $x/L \approx 1$ and $x/L \approx 1.4$. This is the "acceleration zone" we defined in the previous section. The rapid acceleration of ions in turn is colocated with a peak in the electric field [Fig. 5(b)]. This maximum electric field drives a high degree of localized Ohmic heating, which is manifest by a peak in the electron temperature in Fig. 5(c). The magnitude of this maximum value of electron temperature, $T_e = 40$ eV, is consistent with previous studies of magnetically shielded Hall thrusters at this discharge voltage [47]. As Fig. 5(d) shows, the plasma density decays monotonically over the measurement domain. This stems primarily from the acceleration of the ions, increasing velocity at the expense of density.

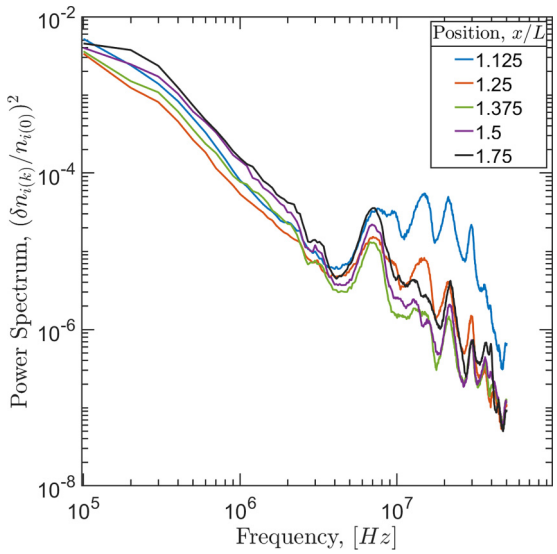

FIG. 6. Power spectra of density oscillations as measured by wave probes as a function of normalized position along the channel centerline.

With respect to measurement uncertainty, we have assumed that the variances in the electric field, temperature, and ion velocity are negligible. These plasma parameters are functions exclusively of moments of the IVDFs, and as outlined in the preceding section, we assume that the error in these moments is negligible based on the precision of the LIF system, which is described in extreme detail in Refs. [41,48]. For the plasma density, however, we include measurement uncertainty as represented by the shaded range of values. This range is dictated by the choice of the downstream boundary condition for ion density in the IBIS method. The mean value we use in this range is $n_{i(0)} \approx 2 \times 10^{17}$ m^3, which is based on our measurement from the ion saturation probe and Eq. (23). However, we also allow for a $\pm 50\%$ variance (cf. [40]) to account for uncertainty in the measurement arising from the probe geometry, sheath expansion, and drifting species. As discussed in Ref. [41], the collision frequency calculated from Eq. (29) and presented in the next section can have appreciable, but difficult to quantify, uncertainty stemming from the underlying assumptions of the IBIS method. In general, however, these uncertainties seem to be below the significant uncertainty introduced from the density measurement.

B. Wave properties

In this section, we consider the two measured wave properties in Eq. (4): the oscillation power spectrum $|\delta n_{i(f)}/n_{i(0)}|^2$ and electron growth rate $\gamma_{e(f)}$. To this end, we first show in Fig. 6 the power spectra inferred by the wave probes as a function of axial location along the channel centerline. In each plot, we see several distinct harmonics visible starting at 4 MHz and every ~7 MHz thereafter. Based on the theoretical dispersion relation, for electric field strengths typical of the acceleration zone, these harmonics correspond to the resonances of the EDI. The frequency content in the range from 1 to 3 MHz is associated with the MTSI. The measured power spectrum in this range decays exponentially with increasing

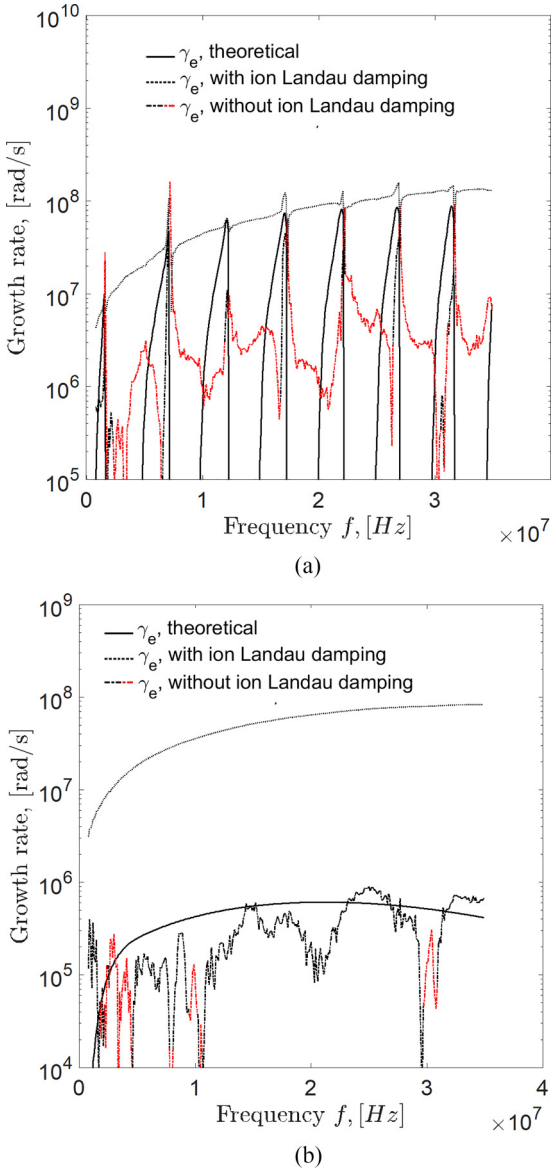

FIG. 7. Absolute value of measured and theoretical growth rates in the (a) acceleration region $x/L = 1.25$, and (b) downstream plume (b) $x/L = 1.75$ (b). Two curves are shown for the measured growth rate for the cases in which the ion growth is zero or driven by ion Landau damping. The growth rate labeled "linear theory" is a theoretical value determined from the solution of the linearized dispersion relation, Eq. (10). The red values denote frequencies where the growth rate becomes negative.

frequency, but there is a minor weak peak at 2.5 MHz. Along the channel centerline, the oscillations are at their strongest in the acceleration zone and decay downstream. These trends in frequency and position are consistent with our previous experimental characterization of the EDI [24]. Physically, these results are consistent with the fact that the dominant source of energy for the EDI is the $E \times B$ drift, which is maximized in this thruster at the location of peak electric field [Fig. 5(b)]. We therefore expect the EDI oscillations to be strongest in the upstream region.

Figure 7 shows examples of the measured and theoretical electron growth rates, $\gamma_{e(f)}$, at two representative locations in the discharge: at $x/L = 1.25$ in the acceleration region, and at $x/L = 1.75$ downstream of the acceleration zone. In these plots, the theoretical value is based on the linear dispersion relation [Eq. (10)], which we evaluate with the background properties from Fig. 5. We have also assumed an axial propagation angle of 15° [$k_x = k_y \sin(15°)$] consistent with previous EDI measurements in Hall thrusters [21,24], and we have prescribed a constant radial wave number equal to the channel width—as observed in recent simulations [13,20,49,50]. We determined the measured values for growth rate from the technique outlined in Secs. II C and II D. We include results where we assume the ion growth is zero ($\gamma_{i(f)} = 0$) and where it is the result of ion Landau damping [Eq. (22)]. For the latter case, we show the results for assuming an ion temperature of 1 eV. When we calculate the anomalous collision frequency in the next section, we consider multiple possible ion temperatures ranging from 0.2 to 3.5 eV based on previous measurements and simulations [30,35,51]. Generally, the variation in the ion temperature shifts the magnitude of the growth rate, but the shape remains the same, as shown in Fig. 7.

In the acceleration region [Fig. 7(a)], the cyclotron harmonics are visible in both the theoretical and the measured growth rate, where we assume ion Landau damping is present. We note, however, that when we assume negligible contributions to the total growth from ion damping, the calculated electron growth is negative at several frequencies. This would physically suggest that at these frequencies the wave is not excited, which is not consistent with our observations of the power spectra. This suggests, therefore, at least in this region, that the neglect of ion damping contributions to the total growth is unphysical.

With that said, in comparing the measured electron contribution to growth with ion Landau damping to the theoretical growth, we see that both trends exhibit peaks consistent with the cyclotron resonances. Physically, this is consistent with the interpretation that the dominant source of energy exchange with the background electron drift occurs at these cyclotron resonances. Notably, we see that our measured electron growth exceeds the theoretical estimate from linearized theory. This is an interesting departure that suggests that the waves are actually able to extract momentum from the Hall drift at a higher rate than the linear prediction. Moreover, in discussing this result in the context of our previous experimental findings [27], we found that the measured azimuthal growth rate, $\gamma_{e(y)}$, was an order of magnitude lower than the theoretical value in this region. The fact that we see a higher level of total electron growth, $\gamma_{e(f)} \gg \gamma_{f(y)}$, thus suggests that the electron growth is largely driven not by the theoretical dispersion but rather by a balance with the rate at which wave energy is lost through convection and damping: $\gamma_{e(f)} \approx \gamma_{i(f)} + \frac{1}{2|X_f|^2}(v_{i(0)}\partial_x|X_f|^2)$. This type of marginally stable state [52] has previously been assumed in numerical and theoretical treatments of the EDI [11].

In the downstream region, we see that the theoretical and measured growth rates no longer exhibit peaks with frequency. Due to the weak electric field, and therefore low $E \times B$ velocity, the cyclotron harmonics do not grow. Instead, the

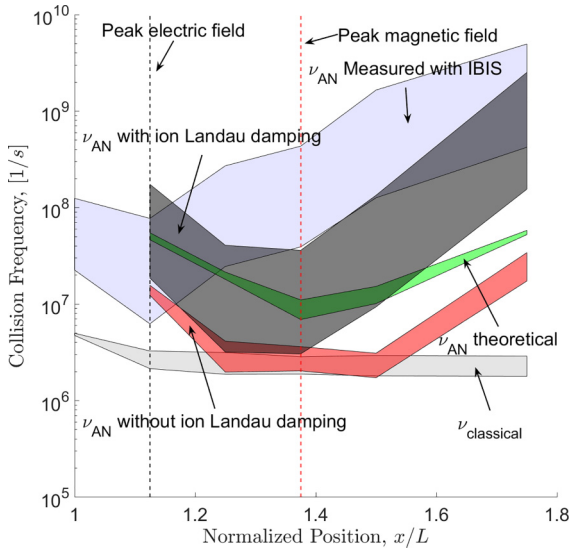

FIG. 8. Anomalous collision frequency determined from LIF and wave measurements as a function of normalized position in the Hall thruster plume. Two wave-driven results are shown based on calculating the electron growth rate with and without including ion Landau damping: ($\gamma_{e(f)} = \gamma_f - \gamma_{i(f)}$ and $\gamma_{e(f)} = \gamma_f$). The theoretical result using the growth rate calculated from Eq. (10) and the classical particle collision frequency are also shown for reference.

dispersion takes on an ion-acoustic-like solution, but importantly this is not the same acoustic limit of the EDI in the case of a large radial wave number. As discussed in the previous section, we assume a radial wave number corresponding to the channel width. For the downstream conditions, this yields a normalized wave number of $k_z\lambda_{De} \sim 0.005$–$0.01$, which is too low to result in the ion acoustic limit of the EDI (see Fig. 2). The observed dispersion is actually the MTSI. For low electric field, the lobe of unstable wave numbers associated with the MTSI broadens substantially such that it is nearly indistinguishable from the ion acoustic solution. We discuss this point further in Sec. V.

We also remark that, as was the case with the upstream dynamics, the growth rate is still largely dominated by a balance with convection and ion Landau damping rather than the linearized growth. In a departure from the upstream measurement, however, we see that the measured growth rate with ion Landau damping exceeds the theoretical growth by an order of magnitude. The disparity between the growth with ion Landau damping in particular shows a marked increase from the upstream case. As we discuss in the following section, this level of disparity is critical for capturing the orders of magnitude change in the anomalous collision frequency.

C. Anomalous collision frequency

We show in Fig. 8 the spatial variation in the classical collision frequency, the measured anomalous collision frequency, and estimates for the wave-contribution to the anomalous collision frequency. We determined the classical collision frequency, $\nu_{classical}$, based on the electron-ion Coulomb rate (cf. [45]) where we used experimental measurements of electron temperature and density (Fig. 5). We inferred the total electron collision frequency through the IBIS method as described in Sec. III B 3. The variation in both the classical and IBIS-measured anomalous collision frequencies stems from the uncertainty in the plasma density. We evaluated the wave-driven contributions to the collision frequency with Eq. (9), where we employed the background plasma parameters measured from the IBIS technique presented in Sec. IV A, the measured power spectra and growth rates shown in Sec. IV B, and terms inferred from the real part of the theoretical EDI dispersion relation given in Eq. (10), where we have assumed that it exists in the acoustic limit. For the case in which we assume that the growth rate does not have a component from ion Landau damping, we omit any contributions from negative growth rates. For the wave-driven collision frequencies, the uncertainty propagates due to the dependence on density in the real part of the dispersion relation and the different assumed ion temperatures in the ion Landau damping term.

As can be seen from Fig. 8, the actual anomalous collision frequency (inferred from the IBIS method) has a minimum value approaching the order of the classical collision frequency at the location of peak electric field ($x/L = 1.125$) and then increases monotonically by over an order of magnitude downstream. This type of spatial variation is consistent with previous measurements [41] and numerical treatments of the anomalous collision frequency [35]. The minimum in collision frequency acts as an effective impedance to cross-field transport, thereby driving the strong electric field in this location. The wave-driven collision frequency in which we use the theoretical growth rate is slightly within the uncertainly of the measured collision frequency in the acceleration zone, but then rapidly decays downstream where it significantly underestimates the actual collision frequency and does not show the correct trends over the axial domain. This result, which is consistent with our previous findings [25], suggests that the theoretical growth rate is not an accurate representation of the interaction of the EDI with the electron drift. Similarly, without considering ion Landau damping, the measured wave-driven anomalous collision frequency underpredicts the actual collision frequency by an order of magnitude, except at the most upstream point. After including ion Landau damping, however, the wave-driven result matches the IBIS values to within the uncertainty at the ends of the axial domain and with only minor disagreement around $x/L = 1.4$. At this location, the wave-driven result underpredicts the collision frequency and is at its minimum value. This occurs due to the wave amplitudes, $|\delta n_i/n_{i(0)}$, having their lowest value at this point (cf. Fig. 6), but the reason for this dip in wave amplitude is unknown at present. The major implication from these results is that experimentally, the wave-driven transport appears to be able to explain the measured magnitude and spatial trends in anomalous collision frequency in a HET. This is a direct experimental indication that this effect is a dominant driver for the electron dynamics in these systems. We discuss the implications and limitations of this conclusion in the following section.

V. DISCUSSION

In the following, we discuss notable aspects of our findings. We first comment on the reasons why the transport

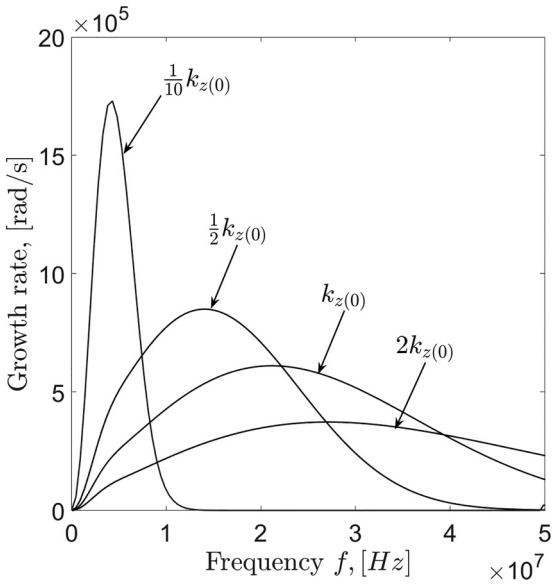

FIG. 9. Linear growth predicted for the EDI by solving the linear dispersion relation for the plasma parameters at the farthest downstream point ($x/L = 1.75$) for different multiples of the radial wave number corresponding to channel width $k_{z(0)}$.

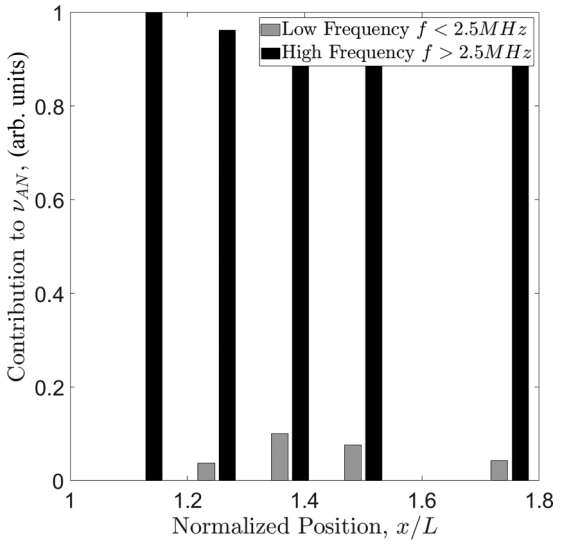

FIG. 10. Relative contribution to anomalous collision frequency for low-frequency oscillations ($f < 2.5$ MHz) and high-frequency oscillations ($f > 2.5$ MHz) at various points in the plume.

calculated with the theoretical growth rate does not match the measured collision frequency in the plasma. As outlined in Ref. [27], this discrepancy stems from the fact that the measured growth in the plasma deviates by an order of magnitude from the theoretical growth. This discrepancy could be attributed to several factors. For instance, as discussed in Refs. [11,20], the growth rate could be modified due to the flattening of the electron velocity distribution function resulting from nonlinear interactions with the waves. Another possibility we consider is that we might have been overly prescriptive in our assumption that the radial wave number remains constant with position. The magnitude and shape of the theoretical growth rate are strongly influenced by this radial wave number, and if the wave number is an order of magnitude smaller, the growth rate would increase proportionally. We illustrate this effect in Fig. 9 by plotting the growth rate for the theoretical dispersion at $x/L = 1.75$ for different values of k_z compared to our assumed wave number, $k_{z(0)}$. Beyond increasing in peak amplitude, the peak growth rate shifts towards lower frequencies as the radial wave number decreases. Consequently, since most of the wave energy in the downstream region originates from the lower frequencies (cf. Fig. 6), these combined effects have a multiplicative influence on the anomalous collision frequency. It is possible that the radial wave number changes as the wave propagates downstream. If this happens, and a large radial wave number persists in the acceleration zone while transitioning to a smaller wave number downstream, there will be closer agreement between the theoretical and measured growth rate. Directly measuring the variation in radial wave number, however, was beyond the scope of this study.

In the context of recent simulations of the EDI, our results validate the importance of the EDI on anomalous transport in Hall thrusters, but we highlight some key differences. While many simulations have demonstrated that the EDI can be sufficient to explain the anomalous transport seen in Hall thrusters, most of these simulations resolve the EDI with an ion-acoustic-like dispersion [11]. Only a subset of simulations have resolved the EDI with distinct harmonics [12,13], and these works also predicted the nonlinear cross-lengthscale energy exchange we observed in Ref. [27]. However, while those simulations did predict EDI-enhanced transport, most of the cross-field electron transport occurred at the low-frequency and long-wavelength features of the EDI—the MTSI component discussed in Sec. II B. In this work, we observe that most of the anomalous transport in the acceleration region occurs due to the oscillations at the high-frequency cyclotron harmonics. To highlight this, we show in Fig. 10 the relative contribution to anomalous transport due to spectral content at frequencies below 2.5 MHz (corresponding to the MTSI) and above 2.5 MHz that represent the EDI cyclotron harmonics. The relative contribution is calculated by performing the summation in Eq. (9) over the frequency range of interest and normalizing by the total summation. In the acceleration zone, there is virtually no influence of the lower frequencies on the cross-field transport. Downstream, the low-frequency oscillations begin to play an increasingly important role, but the high-frequency oscillations remain dominant. However, as we discussed in Sec. IV B, downstream the theoretical dispersion relation predicts that the entire frequency domain is part of the MTSI. Therefore, the distinction between the resonance and MTSI frequencies of the wave requires additional nuance. The cyclotron harmonics of the EDI should predominantly grow and saturate in the acceleration zone. In turn, these oscillations convect downstream where the harmonics remain visible in the wave power spectrum (Fig. 6). Due to either linear growth (Fig. 9) or nonlinear interactions [13,27], the low-frequency oscillations gain energy. Rather than originating from a separate instability, these oscillations are the low-frequency part of the MTSI for the EDI in the downstream plasma conditions. Similarly, the frequencies

associated with the cyclotrons harmonics in the acceleration region become the high-frequency part of the MTSI in the downstream plume. These high-frequency oscillations remain the dominant contribution to anomalous transport. We provide a caveat for these results by noting that our measurement domain for this study did not extend further downstream than $x/L = 1.75$. Previous measurements have shown, however, that the wave energy continues to increase at low frequency further downstream [24]. This implies that the low-frequency waves could become dominant in the far-field plume.

As a final remark, we consider the implications of our results for the development of reduced-fidelity models of anomalous transport, which is particularly relevant for the development of fluid-based predictive models of Hall thrusters [53]. The goal in this case is to find simplified expressions for the anomalous collision frequency that depend on fluid properties. These expressions would approximate the inherently kinetic effects of the waves, allowing these models to be self-consistently incorporated into fluid codes.

To this end, we note that our observations from the preceding sections seem to suggest that the EDI growth in most regions is marginally stable such that the growth is balanced by convection and ion Landau damping. In turn, we note that at both the upstream location where the cyclotron harmonics form and in the downstream plume where the dispersion is of the MTSI, the peak growth rate should occur near the wave number $k_y = 1/\sqrt{2}\lambda_{\mathrm{De}}$. This is apparent in Fig. 2(a), where we see that the strongest cyclotron harmonic mode aligns with $k_y\lambda_{\mathrm{De}} = 1/\sqrt{2}$, which is also the wave number of peak growth for the ion acoustic-limit of the instability. This allows us to prescribe an estimation for the wave number in Eq. (9).

Finally, we note that the power spectra of oscillations appear to be nonlinearly developed, characterized by an inverse power law. As a result, the waves are likely in a saturated state. This suggests in turn that the amplitude of the oscillations may be limited. We consider two limits on the wave energy density, $W = n_{e(0)}T_e|\delta n_i/n_{i(0)}|^2$, consistent with the physical mechanisms that drive the EDI: (i) that the waves are saturated thermally, $W_{\mathrm{thermal}} = \alpha n_{e(0)}T_e$, or (ii) that the waves are saturated in the so-called Fowler limit [54], such that $W_{\mathrm{drift}} = n_{e(0)}m_eV_{E\times B}^2$. Here α and β are constants of proportionality. Subject to these assumptions, the amplitude of the density oscillations should scale as $|\delta n_i/n_{i(0)}|^2 = \alpha$ for thermal saturation and $|\delta n_i/n_{i(0)}|^2 = \beta M_e^2$ for the Fowler limit, where $M_e = V_{E\times B}/V_{\mathrm{the}}$ is the azimuthal electron Mach number. We plot in Fig. 11 the summation of the measured power spectrum $\sum_f |\delta n_{i(f)}/n_{i(0)}|^2$ and the electron Mach number to validate these assumptions. We note that by adding together the amplitudes of the power spectrum, we are converting the broad spectrum into a quasimonochromatic wave. These results shows that the thermal limit is approximately valid for the treatment of the wave amplitude, except at the most upstream point. Interestingly, the Fowler limit only appears valid at the first location where the thermal limit does not hold. This suggests that the wave may initially be saturated by the drift energy in the acceleration region, but in the downstream region the limitation is thermal. Based on these results, and subject to the previous assumptions approximating the wave as monochromatic at $k_{\max} = 1/\sqrt{2}\lambda_{\mathrm{De}}$, we arrive at the

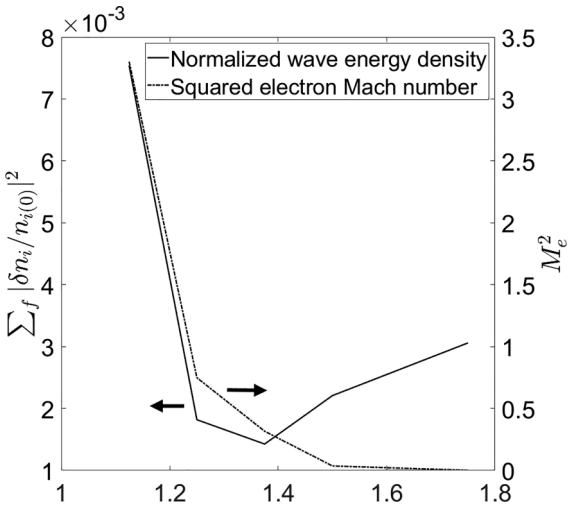

FIG. 11. Measured wave energy density normalized by the thermal energy density: $W/n_{i(0)}T_e = \sum_f |\delta n_i/n_{i(0)}|^2$ and squared azimuthal electron Mach number $M_e^2 = V_{E\times B}^2/V_{\mathrm{the}}^2$.

simplified collision frequency model for thermal and drift energy saturation modes:

$$\nu_{AN(\mathrm{thermal})} = \frac{\omega_{ce}}{E_{x(0)} + \frac{\nabla_x(n_{e(0)}T_e)}{n_{e(0)}}} \frac{\partial \epsilon_r^{(1)}(\vec{k})}{\partial \omega}\bigg|_{k_{\max}} \times \frac{\alpha T_e}{2\sqrt{2}\lambda_D}\left(\frac{\nabla_x(v_{i(0)}n_{e(0)}T_e)}{n_{e(0)}T_e} + \gamma_i\bigg|_{k_{\max}}\right), \quad (31)$$

$$\nu_{AN(\mathrm{drift})} = \frac{\omega_{ce}}{E_{x(0)} + \frac{\nabla_x(n_{e(0)}T_e)}{n_{e(0)}}} \frac{\partial \epsilon_r^{(1)}(\vec{k})}{\partial \omega}\bigg|_{k_{\max}} \times \frac{\beta M_e^2 T_e}{2\sqrt{2}\lambda_D}\left(\frac{\nabla_x(v_{i(0)}n_{i(0)}V_{E\times B}^2)}{n_{e(0)}V_{E\times B}^2} + \gamma_i\bigg|_{k_{\max}}\right). \quad (32)$$

Here we assume that the growth rate is given by the combination of wave energy convection, $\nabla_x(v_{i(0)}W)/W$, and ion Landau damping at the selected number, $\gamma_i|_{k_{\max}}$.

Based on our measured power spectrum, we estimate $\alpha = 0.002$ and $\beta = 0.0023$. The value of α was chosen to best fit the downstream points where $\sum_f |\delta n_{i(f)}/n_{i(0)}|^2$ is approximately constant. In contrast, β was selected based on measurements in the acceleration zone where the Fowler limit appears to hold. Figure 12 shows the resulting collision frequency profiles juxtaposed with the measured IBIS results. The thermal model aligns with the IBIS values within the margin of uncertainty at all points, albeit with slightly worse agreement at the most upstream point. This close alignment underscores the potential usefulness of this experimentally informed model as closure for the ECDI's impact on wave dynamics. Conversely, the drift energy model fails to accurately reproduce the anomalous collision frequency amplitude or spatial trends, with the exception of the first point. At this location, which overlaps with the peak electric field, the drift model corresponds more closely with the IBIS results than does the thermal model. This observation supports the hypothesis that the saturation mechanism varies throughout the plume.

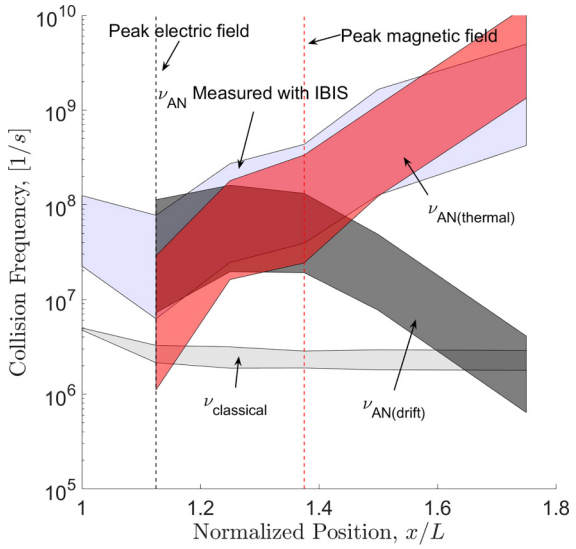

FIG. 12. Anomalous collision frequency for the simplified models based on thermal or drift energy saturation [Eqs. (31) and (32)] as a function of normalized position in the Hall thruster plume. The measured IBIS result and the classical particle collision frequency are also shown for reference.

With regard to the development of simplified fluid codes, these results demonstrate a promising approach, albeit with some important limitations. Both Eqs. (31) and (32) can be solved using solely fluid plasma parameters to self-consistently calculate the anomalous collision frequency. Indeed, the values calculated as shown in Fig. 12 suggest that this approach should yield promising simulation results. Given the superior performance of the drift model in the acceleration zone, it might be beneficial to divide the axial grid into domains, each utilizing different wave energy saturation models. A similar approach has been employed in the past with moderate success [55]. However, it is crucial to note that our model does not extend into the thruster channel and may not adequately reproduce the inflection point in anomalous collision frequency observed at the location of peak electric field. The challenge of accurately and noninvasively probing this region to measure wave properties complicates the experimental validation of various reduced-order wave models.

In summary, we utilized a bispectral analysis technique combined with the assumption that ion Landau damping is non-negligible to infer the electron growth rate and wave energy at several positions in the Hall thruster plume. We employed in turn a quasilinear framework to relate these measured wave properties to an effective wave-driven collision frequency. For much of the measurement domain, the wave-driven collision frequency showed agreement with many of the spatial trends of the collision frequency profile that we inferred from LIF measurements, and the amplitudes were within an order of magnitude. The agreement stems predominately from the inclusion of ion Landau damping in our model of the EDI growth rate. Without ion Landau damping, the measured growth rate resulted in a collision frequency profile that is over an order of magnitude too low in amplitude. Furthermore, the collision frequency profile determined using the theoretical growth rate of the EDI did not agree in magnitude or shape. Overall, our result ultimately provides the long desired experimental evidence demonstrating that the electron drift instability is sufficient to explain the anomalous transport seen in Hall thrusters.

VI. CONCLUSION

In this work, we have performed a direct calculation of wave-driven anomalous collision frequency in a Hall effect thruster. These experimental results demonstrate that the electron drift instability can adequately describe the observed anomalous cross-field transport. However, some ambiguity still exists between simulation and experiment. Notably, our results indicate that anomalous transport is primarily driven by the high-frequency EDI cyclotron harmonics, whereas some simulations suggest that the transport is mostly driven by either an ion-acoustic-like form of the EDI or the low-frequency MTSI component. From a practical perspective, our findings suggest that there may be simple, experimentally informed assumptions available to represent the impact of wave dynamics on the anomalous collision frequency effectively. These assumptions can, in turn, be embodied in simplified models for transport. Such models could principally be incorporated into lower-fidelity, fluid-based Hall thruster models, allowing for the capture of wave-driven transport without the need for resolving the EDI in high-fidelity simulations. These approximations could potentially unlock predictive capabilities with low computational cost. Finally, from a practical perspective, our findings suggest that there may be simple, experimentally informed assumptions for how we can represent the impact of the wave dynamics on the anomalous collision frequency.

ACKNOWLEDGMENTS

This material is based upon work supported by the AFOSR Space Propulsion and Power program through a Young Investigator Award, FA9550-19-1-0022 and by the U.S. Department of Energy, Office of Science, Office of Fusion Energy Sciences, under the Early Career Research Program Award, DE-SC002298.

[1] G. S. Janes and R. S. Lowder, Anomalous Electron Diffusion and Ion Acceleration in a Low-Density Plasma, Phys. Fluids **9**, 1115 (1966).

[2] J. P. Boeuf, Tutorial: Physics and modeling of Hall thrusters, J. Appl. Phys. **121**, 011101 (2017).

[3] N. B. Meezan, W. A. Hargus, and M. A. Cappelli, Anomalous electron mobility in a coaxial Hall discharge plasma, Phys. Rev. E **63**, 026410 (2001).

[4] I. D. Kaganovich, A. Smolyakov, Y. Raitses, E. Ahedo, I. G. Mikellides, B. Jorns, F. Taccogna, R. Gueroult, S. Tsikata, A.

Bourdon, J.-P. Boeuf, M. Keidar, A. T. Powis, M. Merino, M. Cappelli, K. Hara, J. A. Carlsson, N. J. Fisch, P. Chabert, I. Schweigert *et al.*, Physics of E × B discharges relevant to plasma propulsion and similar technologies, Phys. Plasmas **27**, 120601 (2020).

[5] C. Boniface, L. Garrigues, G. J. M. Hagelaar, J. P. Boeuf, D. Gawron, and S. Mazouffre, Anomalous cross field electron transport in a Hall effect thruster, Appl. Phys. Lett. **89**, 161503 (2006).

[6] S. Barral, K. Makowski, Z. Peradzyński, N. Gascon, and M. Dudeck, Wall material effects in stationary plasma thrusters. II. Near-wall and in-wall conductivity, Phys. Plasmas **10**, 4137 (2003).

[7] N. Gascon, M. Dudeck, and S. Barral, Wall material effects in stationary plasma thrusters. I. Parametric studies of an SPT-100, Phys. Plasmas **10**, 4123 (2003).

[8] M. S. McDonald and A. D. Gallimore, Parametric investigation of the rotating spoke instability in Hall thrusters, in *32nd International Electric Propulsion Conference* (Electric Rocket Propulsion Society, Cleveland, OH, 2011).

[9] C. L. Ellison, Y. Raitses, and N. J. Fisch, Cross-field electron transport induced by a rotating spoke in a cylindrical Hall thruster, Phys. Plasmas **19**, 013503 (2012).

[10] J. P. Boeuf and A. Smolyakov, Preface to special topic: Modern issues and applications of E × B plasmas, Phys. Plasmas **25**, 061001 (2018).

[11] T. Lafleur, S. D. Baalrud, and P. Chabert, Theory for the anomalous electron transport in Hall effect thrusters: I. insights from particle-in-cell simulations, Phys. Plasmas **23**, 053502 (2016).

[12] S. Janhunen, A. Smolyakov, O. Chapurin, D. Sydorenko, I. Kaganovich, and Y. Raitses, Nonlinear structures and anomalous transport in partially magnetized E × B plasmas, Phys. Plasmas **25**, 011608 (2018).

[13] S. Janhunen, A. Sydorenko, D. Sydorenko, M. Jimenez, I. Kaganovich, and Y. Raitses, Evolution of the electron cyclotron drift instability in two-dimensions, Phys. Plasmas **25**, 082308 (2018).

[14] A. L. Ortega, I. Katz, and V. H. Chaplin, A first-principles model based on saturation of the electron cyclotron drift instability for electron transport in hydrodynamic simulations of Hall thruster plasmas, in *35th International Electric Propulsion Conference* (Electric Rocket Propulsion Society, Cleveland, OH, 2017).

[15] J. P. Boeuf and L. Garrigues, E × B electron drift instability in Hall thrusters: Particle-in-cell simulations vs theory, Phys. Plasmas **25**, 061204 (2018).

[16] A. Héron and J. C. Adam, Anomalous conductivity in Hall thrusters: Effects of the non-linear coupling of the electron-cyclotron drift instability with secondary electron emission of the walls, Phys. Plasmas **20**, 082313 (2013).

[17] I. Katz, V. H. Chaplin, and A. L. Ortega, Numerical studies of Hall thruster acceleration region electron transport, in *2018 Joint Propulsion Conference, AIAA Propulsion and Energy Forum* (AIAA, 2018).

[18] A. Ducrocq, J. C. Adam, and A. Heron, High-frequency electron drift instability in the cross-field configuration of Hall thrusters, Phys. Plasmas **13**, 102111 (2006).

[19] J. Cavalier, N. Lemonie, G. Bonhomme, S. Tsikata, C. Honore, and D. Gresillon, Hall thruster plasma fluctuations identified as the E × B electron drift instability: Modeling and fitting on experimental data, Phys. Plasmas **20**, 082107 (2013).

[20] T. Lafleur, S. D. Baalrud, and P. Chabert, Theory for the anomalous electron transport in Hall effect thrusters: II. Kinetic model, Phys. Plasmas **23**, 053503 (2016).

[21] S. Tsikata, N. Lemoine, V. Pisarev, and D. M. Gresillon, Dispersion relation of electron density fluctuations in a Hall thruster plasma, observed by collective light scattering, Phys. Plasmas **16**, 033506 (2009).

[22] S. Tsikata, C. Honore, N. Lemoine, and D. M. Gresillon, Three-dimensional structure of electron density fluctuations in the Hall thruster plasma: E × B mode, Phys. Plasmas **17**, 112110 (2010).

[23] Z. A. Brown and B. A. Jorns, Dispersion relation measurements of plasma modes in the near-field plume of a 9-kW magnetically shielded thruster, in *35th International Electric Propulsion Conference* (Electric Rocket Propulsion Society, Cleveland, OH, 2017).

[24] Z. A. Brown and B. A. Jorns, Spatial evolution of small wavelength fluctuations in a Hall thruster, Phys. Plasmas **26**, 113504 (2019).

[25] Z. Brown and B. Jorns, Experimental measurements of the contribution of plasma turbulence to anomalous collision frequency in a Hall thruster, in *AIAA Propulsion and Energy 2021 Forum* (AIAA, 2021).

[26] A. Tavassoli, A. Smolyakov, M. Shoucri, and R. J. Spiteri, Nonlinear regimes of the electron cyclotron drift instability in Vlasov simulations, Phys. Plasmas **29**, 030701 (2022).

[27] Z. A. Brown and B. A. Jorns, Growth and saturation of the electron drift instability in a crossed-field plasma, Phys. Rev. Lett. **130**, 115101 (2023).

[28] Z. A. Brown, Small-scale instability driven electron transport in Hall thrusters, Ph.D. thesis, University of Michigan, 2022 (Unpublished).

[29] R. Davidson and N. Krall, Anomalous transport in high-temperature plasmas with applications to solenoidal fusion systems, Nucl. Fusion **17**, 1313 (1977).

[30] T. Lafleur, P. Chabert, and A. Bourdon, Anomalous electron transport in Hall-effect thrusters: Comparison between quasi-linear kinetic theory and particle-in-cell simulations, Phys. Plasmas **25**, 061202 (2018).

[31] Ch. P. Ritz, E. J. Powers, and R. Bengtson, Experimental measurement of three-wave coupling and energy cascading, Phys. Fluids B **1**, 153 (1989).

[32] J. S. Kim, R. Durst, R. Fonck, E. Fernandez, A. Ware, and P. W. Terry, Technique for the experimental estimation of nonlinear energy transfer in fully developed turbulence, Phys. Plasmas **3**, 3998 (1996).

[33] R. Z. Sagdeev and A. A. Galeev, *Nonlinear Plasma Theory* (Benjamin, New York, 1969).

[34] C. Ritz and E. Powers, Estimation of nonlinear transfer functions for fully developed turbulence, Physica D **20**, 320 (1986).

[35] I. G. Mikellides, B. Jorns, I. Katz, and A. L. Ortega, Hall simulations with a first-principles electron transport model based on the electron cyclotron drift instability, in *52nd AIAA/SAE/ASEE Joint Propulsion Conference* (AIAA, Salt Lake City, Utah, 2012).

[36] R. Martorelli, T. Lafleur, A. Bourdon, and P. Chabert, Comparison between ad-hoc and instability-induced electron anomalous transport in a 1d fluid simulation of Hall-effect thruster, Phys. Plasmas **26**, 083502 (2019).

[37] R. R. Hofer, S. E. Cusson, and R. B. Lobbia, The h9 magnetically shielded Hall thruster, in *35th International Electric Propulsion Conference* (Electric Rocket Propulsion Society, Cleveland, OH, 2017).

[38] S. E. Cusson, R. R. Hofer, R. B. Lobbia, B. A. Jorns, and A. Gallimore, Performance of the H9 magnetically shielded Hall thrusters, in *35th International Electric Propulsion Conference* (Electric Rocket Propulsion Society, Cleveland, OH, 2017).

[39] I. G. Mikellides, I. Katz, R. Hofer, and D. Goebel, Magnetic shielding of walls from the unmagnetized ion beam in a Hall thruster, Appl. Phys. Lett. **102**, 023509 (2013).

[40] R. B. Lobbia and B. E. Beal, Recommended practice for use of Langmuir probes in electric propulsion testing, J. Propul. Power **33**, 566 (2017).

[41] E. T. Dale and B. A. Jorns, Non-invasive time-resolved measurements of anomalous collision frequency in a Hall thruster, Phys. Plasmas **26**, 013516 (2019).

[42] B. A. Jorns, D. M. Goebel, and R. R. Hofer, Plasma perturbations in high-speed probing of Hall thruster discharge chambers: Quantification and mitigation, in *51st AIAA/SAE/ASEE Joint Propulsion Conference* (AIAA, 2015).

[43] L. Grimaud, A. Pétin, J. Vaudolon, and S. Mazouffre, Perturbations induced by electrostatic probe in the discharge of Hall thrusters, Rev. Sci. Instrum. **87**, 043506 (2016).

[44] J. Pérez-Luna, G. J. M. Hagelaar, L. Garrigues, and J. P. Boeuf, Method to obtain the electric field and the ionization frequency from laser induced fluorescence measurements, Plasma Sources Sci. Technol. **18**, 034008 (2009).

[45] D. Goebel and I. Katz, *Fundamentals of Electric Propulsion: Ion and Hall Thrusters* (Wiley, 2008).

[46] W. Huang, A. D. Gallimore, and R. R. Hofer, Neutral flow evolution in a six-kilowatt Hall thruster, J. Propul. Power **27**, 553 (2011).

[47] R. R. Hofer, D. M. Goebel, I. G. Mikellides, and I. Katz, Magnetic shielding of a laboratory Hall thruster. II. Experiments, J. Appl. Phys. **115**, 043304 (2014).

[48] E. Dale, Investigation of the Hall Thruster Breathing Mode, Ph.D. thesis, University of Michigan, 2019.

[49] M. Sengupta and A. Smolyakov, Mode transitions in nonlinear evolution of the electron drift instability in a 2d annular E × B system, Phys. Plasmas **27**, 022309 (2020).

[50] F. Taccogna, P. Minelli, Z. Asadi, and G. Bogopolsky, Numerical studies of the ExB electron drift instability in Hall thrusters, Plasma Sources Sci. Technol. **28**, 064002 (2019).

[51] I. Katz, A. L. Ortega, B. A. Jorns, and I. G. Mikellides, Growth and saturation of ion acoustic waves in Hall thrusters, in *52nd AIAA Joint Propulsion Conference* (AIAA, 2016).

[52] W. M. Manheimer and J. P. Boris, Self-consistent theory of a collisionless resistive shock, Phys. Rev. Lett. **28**, 659 (1972).

[53] B. Jorns, Predictive, data-driven model for the anomalous electron collision frequency in a Hall effect thruster, Plasma Sources Sci. Technol. **27**, 104007 (2018).

[54] T. K. Fowler, Bounds on plasma instability growth rates, Phys. Fluids **7**, 249 (1964).

[55] R. R. Hofer, I. Katz, I. G. Mikallides, D. M. Goebel, K. K. Jameson, R. M. Sullivan, and L. K. Johnson, Efficacy of electron mobility models in hybrid-PIC Hall thruster simulations, in *Proceedings of the 44th AIAA/ASME/SAE/ASEE Joint Propulsion Conference* (AIAA, 2008).